THE EFFECT OF SPACECRAFT CHARGING ON LOW-ENERGY ION MEASUREMENTS AROUND COMET 67P/CHURYUMOV-GERASIMENKO

SOFIA BERGMAN

Licentiate Thesis

Swedish Institute of Space Physics
Kiruna, Sweden

Department of Physics
Faculty of Science and Technology
Umeå University
Umeå, Sweden

Supervisors:
Gabriella Stenberg Wieser
Martin Wieser
Gert Brodin

February 2020

ABSTRACT

A spacecraft in space interacts with the surrounding environment and aqcuires an electrostatic potential. Charged particles are constantly bombarding the surface of the spacecraft, and at the same time solar EUV radiation induces photoemission, causing electrons to be emitted from the surface. The result is a transfer of charge between the environment and the spacecraft surface, and the surface charges to a positive or negative potential. The charged surface can cause interferences with scientific instruments on board. In this thesis, we investigate how spacecraft charging affects low-energy ion measurements. The Rosetta spacecraft visited comet 67P/Churyumov-Gerasimenko between the years 2014-2016. On board the spacecraft, the Ion Composition Analyzer (ICA) was measuring positive ions in the environment around the comet with the aim of investigating the interaction between cometary particles and the solar wind. Important for this interaction is ions with a low energy. Measuring these ions is, however, difficult due to the charged spacecraft surface. Rosetta was commonly charged to a negative potential, and consequently the measured positive ions were accelerated toward the surface before detection, affecting both their energy and travel direction. In this thesis, we study how the changed travel directions affected the effective field of view (FOV) of the instrument. We use the Spacecraft Plasma Interaction Software (SPIS) to simulate the spacecraft plasma interactions and the ion trajectories around the spacecraft. The results show that the FOV of ICA is severely distorted at low ion energies, but the distortion varies between different viewing directions of the instrument and is dependent on the properties of the surrounding plasma.

SAMMANFATTNING

En rymdfarkost i rymden växelverkar med omgivningen och laddas upp till en elektrostatisk potential. Laddade partiklar från omgivningen kolliderar ständigt med farkostens yta, och samtidigt inducerar EUV-strålning från solen fotoemission, vilket gör att fotoelektroner emitteras från ytan. Laddning överförs då mellan omgivningen och ytan på farkosten, och ytan laddas upp till en positiv eller negativ potential. Den laddade ytan påverkar mätningar som görs av vetenskapliga instrument ombord på farkosten. I denna avhandling undersöker vi hur farkostpotentialen har påverkat mätningar av lågenergijoner. Rymdfarkosten Rosetta studerade komet 67P/Tjurjumov-Gerasimenko mellan åren 2014-2016. Jonmasspektrometern ICA mätte positiva joner i omgivningen runt kometen, med syfte att studera hur kometjoner växelverkar med solvinden. Joner med låg energi är viktiga i denna interaktion. På grund av den uppladdade farkosten är det dock svårt att mäta dessa joner. Rosetta var oftast uppladdad till en negativ potential under missionen, och de positiva jonerna som ICA observerade accelererades därför mot farkosten innan de detekterades, vilket ledde till att både deras energi och färdriktning förändrades. I denna avhandling studerar vi hur ICAs effektiva synfält har förändrats på grund av de förändrade partikelbanorna. Vi använder programvaran SPIS (Spacecraft Plasma Interaction Software) för att simulera växelverkan mellan farkosten och omgivningen och uppladdningen av ytan. Vi studerar sen hur jonerna rör sig genom den resulterande potentialfördelningen i omgivningen. Resultaten visar att ICAs synfält är förvrängt vid låga jonenergier, men effekten varierar mellan olika tittriktningar och påverkas av egenskaperna hos det omgivande plasmat.

Bergman, S., Stenberg Wieser, G., Wieser, M., Johansson, F. L., & Eriksson, A. (2020). The influence of spacecraft charging on low-energy ion measurements made by RPC-ICA on Rosetta. *Journal of Geophysical Research: Space Physics*, 125(1). doi:10.1029/2019JA027478

Bergman, S., Stenberg Wieser, G., Wieser, M., Johansson, F. L., & Eriksson, A. (2020). The influence of varying spacecraft potentials and Debye lengths on in situ low-energy ion measurements. Submitted to *Journal of Geophysical Research: Space Physics*

ACKNOWLEDGMENTS

CONTENTS

INTRODUCTION

Ever since the launch of Sputnik in 1957 mankind has continuously sent spacecraft to space. This paved the way for the development of new technologies here on Earth, and also the exploration of the Universe. Sending a spacecraft to space is, however, not easy. When the spacecraft leaves the surface of Earth, it is exposed to the harsh space environment (Tribble, 2003). Radiation can then penetrate the surface of the spacecraft and cause damage to the material underneath, and small, less energetic, particles can interact directly with the surface causing sputtering and chemical erosion. Larger particles, like dust, micrometeoroids and manmade debris, also pose an immediate threat to the spacecraft. A dominating part of the particles present in space are charged particles, existing in the form of *plasma*. A plasma consists of ions and free electrons, and is, together with solid, liquid and gas, one of the four fundamental states of matter. The interaction of the charged particles in the plasma with the spacecraft surface results in another problematic effect, which is the topic of this thesis: an accumulation of charge on the spacecraft surface.

Spacecraft charging has been discussed ever since the birth of the spaceflight era. Already in 1955 complications connected to spacecraft charging were discussed in a paper by Johnson and Meadows (1955), who analyzed data from a rocket-borne mass spectrometer. Since then the understanding of this phenomenon has successively increased. The theory behind spacecraft charging will be outlined in Chapter 4, but the resulting outcome is that the spacecraft surface acquires an electrostatic potential with respect to the plasma, which can be either positive or negative. If different parts of the spacecraft charge to different potentials, known as differential charging, discharges can occur if the potential difference is large enough. This can seriously damage onboard systems and electronics, and due to the high damaging risk the field of differential charging and discharges receives a great amount of attention. There are, however, other problems arising due to spacecraft charging. One of them is the interference with scientific instruments onboard the spacecraft. Even though this is very problematic for, especially, instruments measuring low-energy charged particles, this area has received much less attention.

Many instruments on board different spacecraft suffer from interferences caused by a charged spacecraft surface. In this thesis, we focus on the Ion Composition Analyzer (ICA, Nilsson et al., 2007) on board Rosetta (Glassmeier et al., 2007a). Rosetta followed comet 67P/Churyumov-Gerasimenko for two years, providing unique measurements of a comet nucleus and the surrounding environment. ICA

was measuring positive ions in the vicinity of the comet, with the aim of studying the interaction between the cometary particles and the solar wind. ICA can measure ion energies down to just a few eV, but unfortunately the low-energy part of the obtained data is heavily distorted by the spacecraft potential. Rosetta was charged to a negative potential during the major part of the mission, which means that the positive ions measured by ICA were accelerated toward the spacecraft surface prior to detection. This affected both their energy and direction of travel.

In this thesis, we use the simulation software SPIS (Spacecraft Plasma Interaction Software) to study how the changed travel directions of the ions have affected the effective field of view (FOV) of ICA. The ultimate goal is to develop a method to reconstruct the data, to find the original travel direction of the ions.

2

COMETS AND ROSETTA

2.1 PHYSICAL PROPERTIES OF COMETS

Comets have long fascinated us humans. Comets passing close to Earth can be visible to the naked eye, and hence they have been observed for thousands of years. The celestial nature of these objects was, however, not realized until the 1600s, until when they were thought to be meteorological phenomena with an origin in the atmosphere of Earth (Festou, Rickman, and West, 1993). They were thought to be bad omens bringing natural catastrophes and sickness to the people of Earth. Today we know that these icy bodies in fact are remnants from the creation of the Solar System (Meierhenrich, 2015). They are assumed to have been formed in the outer regions of the solar nebula, where the temperature was low enough to keep ice in the cometary nuclei. Comets are assumed to have changed relatively little since their formation, and have hence preserved the chemical characteristics of its material. They are therefore interesting objects, possibly yielding information about the creation and evolution of the Solar System.

2.1.1 *Nucleus*

The comet nucleus is a small, irregularly shaped object, consisting of ice and dust. The crust is very dark. Comet 67P, for example, has an albedo of ~6% (Capaccioni et al., 2015), which makes them some of the darkest objects ever observed in the Solar System. The ice in the nucleus is mainly water ice, with some other frozen gases such as CO_2, CO, CH_4 and NH_3. Silicates and organic material dominate the dusty and rocky part of the nucleus.

2.1.2 *Coma*

When a comet approaches the Sun the ice in the nucleus starts to sublimate, creating an atmosphere called a *coma*. The gas particles drag dust particles along with them from the surface, and the coma hence contains both gas and dust. Due to the low gravity the newly released particles quickly escape the nucleus, creating a coma which might be several millions of km large. The neutral gas particles get ionized and start interacting with the solar wind (Cravens and Gombosi, 2004). The dominating ionizing process is photoionization by solar radiation, but charge exchange with the solar wind and electron impact ionization are also important. The newly born ions are

accelerated by the convective electric field of the solar wind, and become "pick-up" ions in the solar wind flow. This process is commonly referred to as *mass loading* (Szegö et al., 2000).

2.1.3 *Tails*

Comets are probably mostly known for their tails. The *plasma tail*, or *ion* tail, consists of molecular ions and electrons and points more or less in the antisunward direction due to its interaction with the solar wind. The *dust tail* is composed of dust particles. Two main forces are acting on the particles in this tail: the solar radiation pressure and the solar gravity. Radiation pressure mainly affects the smaller particles, pushing them in the antisunward direction, while larger particles to a greater extent are affected by the solar gravity and are drawn towards the orbit of the comet. This causes a rather broad, curved, tail, pointing in a slightly different direction than the plasma tail.

2.1.4 *Magnetic field*

Comets do not have intrinsic magnetic fields (Auster et al., 2015), and hence the only magnetic field present in the vicinity of the comet is the interplanetary magnetic field (IMF). The IMF is frozen into the solar wind. Due to the mass loading of cometary ions into the solar wind flow, the solar wind slows down when encountering the comet. If the outgassing of cometary particles is high enough this results in a draping of the magnetic field around the comet. Close to the comet nucleus a magnetic field free region is formed, the *diamagnetic cavity* (Goetz et al., 2016a, 2016b).

2.2 ROSETTA

Numerous spacecraft have visited comets in the past. Some examples are the visits to comet 1P/Halley by Vega-1 and Vega-2, Sakigake, Suisei and Giotto in 1986, and the later visits to 19P/Borrelly, 81P/Wild, 9P/Tempel and 103P/Hartley by Deep Space 1, Stardust, Deep Impact and EPOXI. These are all important missions providing the first insights into the nature of comets. What these missions have in common, however, is that they only provided flybys of the comet, often with a large relative velocity and/or at a large distance from the comet nucleus. The obtained data are, as a consequence, limited.

The Rosetta mission was born with the aim to provide a more detailed analysis of a comet nucleus and its environment. In 1993 the mission was approved and the launch took place in March 2004 from the Guyana Space Center in French Guyana. The originally planned target was comet 46P/Wirtanen, but due to a delayed launch the

target was changed to comet 67P/Churyumov-Gerasimenko. Rosetta arrived at comet 67P in August 2014, after ten years in space. At this point the comet was at a heliocentric distance of more than 3.6 AU. Rosetta followed the comet through the solar system for two years as it approached the Sun, reached its perihelion and continued its journey outwards again. It hence became the first spacecraft to ever orbit a comet nucleus and the first spacecraft to follow a comet for an extended amount of time and hence provide measurements during different levels of comet activity. Rosetta was also the first spacecraft to ever land a probe on a comet surface. On November 2014 the probe, Philae, was deployed and landed on the surface. Despite problems with the landing, Philae managed to provide a couple of days of unique science from the nucleus. The whole mission ended in September 2016 by impacting the spacecraft onto the comet nucleus.

The Rosetta payload comprised 11 instruments on the orbiter (Figure 2.1), and 10 on the lander (Figure 2.2). The instruments on the orbiter included imaging spectrometers, microwave and radio instruments, in situ instruments to study dust and volatiles, and plasma instruments. The lander carried instruments suited for a detailed study of the structure and composition of the surface and subsurface of the nucleus. On board the orbiter, the Rosetta Plasma Consortium (RPC, Carr et al., 2007) was a suite of plasma instruments designed to make in situ measurements of the plasma environment around the comet. It consisted of five instruments: the Ion and Electron Sensor (IES, Burch et al., 2007), the Ion Composition Analyzer (ICA, Nilsson et al., 2007), the Langmuir Probes (LAP, Eriksson et al., 2007), the Mutual Impedance Probe (MIP, Trotignon et al., 2007) and the Magnetometer (MAG, Glassmeier et al., 2007b). ICA was designed and built by the Swedish Institute of Space Physics in Kiruna, Sweden, and is the instrument targeted in this thesis.
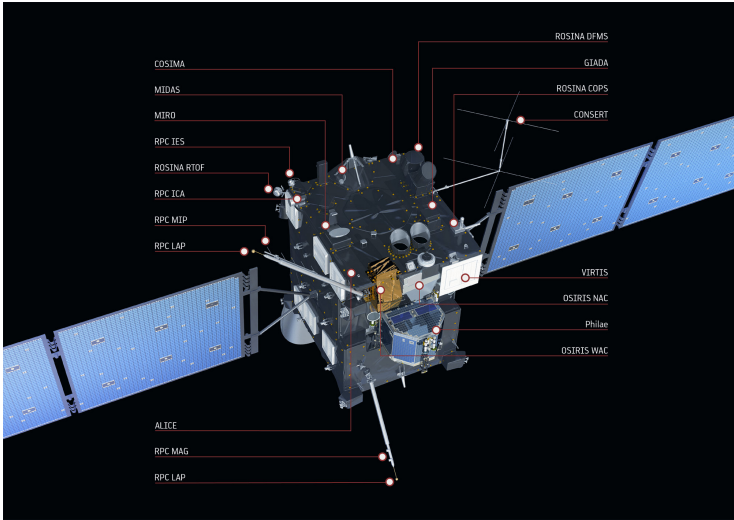
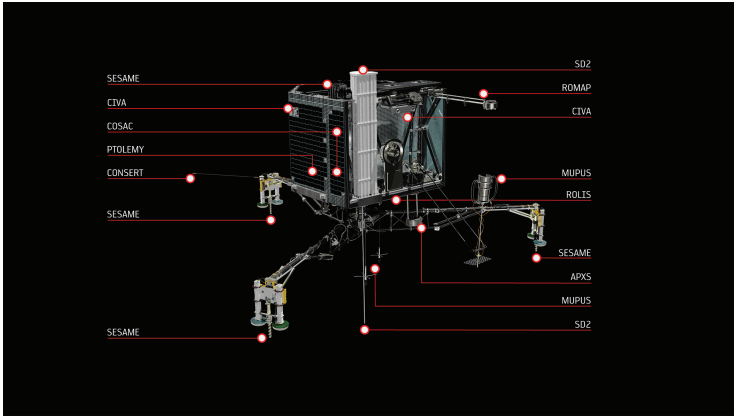Figure 2.1: The Rosetta orbiter with instruments. Copyright: ESA/ATG medialab.

Figure 2.2: The Philae lander with instruments. Copyright: ESA/ATG medialab.

THE ION COMPOSITION ANALYZER

The Ion Composition Analyzer (ICA) is a mass resolving ion spectrometer measuring positive ions. The design is that of a spherical "top-hat" electrostatic analyzer. The basic design is illustrated in Figure 3.1. An incoming ion first encounters the deflection system, controlling the elevation angle φ. Only particles with a certain elevation angle are guided into the instrument. This is done by two plates put to different electrostatic potentials (U_1 and U_2 in Figure 3.1), and the elevation angle is controlled by changing the potential difference between the plates. The instrument accepts particles arriving within an angle of $\pm 45°$ with respect to the aperture plane. This range is divided into 16 steps, where the resolution of one step is 5.625°. The ions passing through the deflection system enter the electrostatic analyzer (ESA), analyzing the energy of the ions. This part of the instrument consists of two spherical electrodes, one inner and one outer, put to different potentials (U_{inner} and U_{outer} in Figure 3.1). An electric field is generated between the plates, and only particles within a prescribed energy passband pass through the ESA. This passband is controlled by changing the potentials of the electrodes. The instrument covers an energy range of a few eV/q to 40 keV/q with a nominal resolution of $\Delta E/E = 0.07$. The particles are accelerated into the ESA which affects the resolution at low energies, and below 30 eV the resolution decreases to $\Delta E/E = 0.30$. The energy range is divided into 96 exponentially spaced steps, which is stepped through during one measurement cycle. The full energy range is covered in 12 seconds, which means that a full scan takes 192 seconds (12 seconds times 16 elevation steps). After passing through the ESA the ions arrive at the mass analyzer. In this part of the instrument magnets are used to create a cylindrical magnetic field, sorting the ions according to their momentum per charge. Heavier species follow a straighter trajectory through the filter and end up on a different area of the detector. Post-acceleration of the ions into this part of the instrument is possible, which can be used to adjust the mass resolution for heavy and light species. The ions will finally hit a circular MCP and create an electron shower, which is detected by an anode system. The anode system consists of 32 rings and 16 sectors, to measure the radial and azimuthal impact position, respectively. The radial impact position corresponds to mass while the azimuthal impact position corresponds to the azimuthal arrival direction of the ion.

3.1   FIELD OF VIEW

The total nominal field of view (FOV) of ICA is 360° × 90° as illustrated in Figure 3.2. In the azimuthal direction (nominal FOV of 360°) the FOV is divided into 16 sectors, as illustrated in Figure 3.2b. Each sector covers an angle of 22.5°, which is the nominal resolution of the instrument in this direction. 0° azimuth is defined to be between sectors 8 and 9 and the angle is measured in the clockwise direction, when looking at the instrument in the -y direction. As already mentioned, the elevation angle is also determined. The total FOV is 90° in this direction, and this range is divided into 16 elevation steps. Elevation bin 0 is defined to be towards the spacecraft body, -45° from the aperture plane. One individual instrument pixel (i.e. one elevation bin of one sector) hence has a nominal FOV of 22.5° × 5.625°.
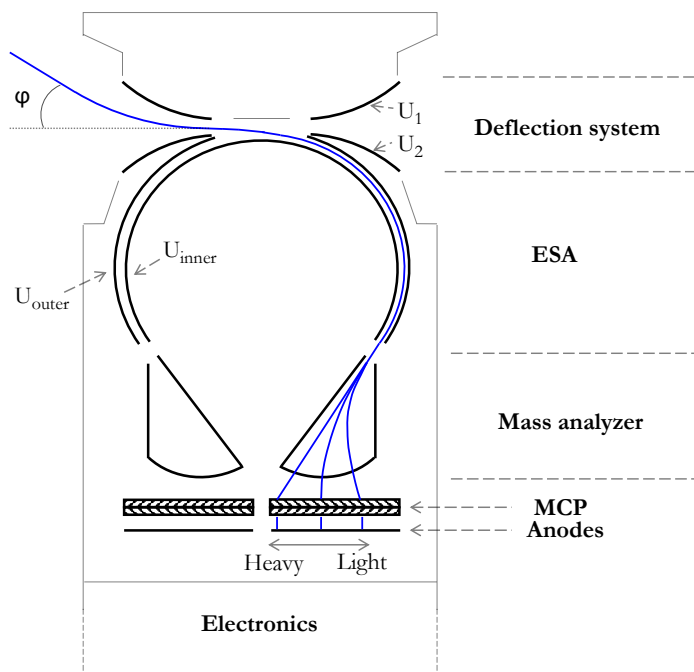
Figure 3.1: Sketch illustrating the basic design of ICA.

a)

elevation

45°   -45°

z

y

b)

z

x

6 5 4 3
7   2   22.5°
8   1
azimuth 0° / 360°
9   0
10   15
11 12 13 14
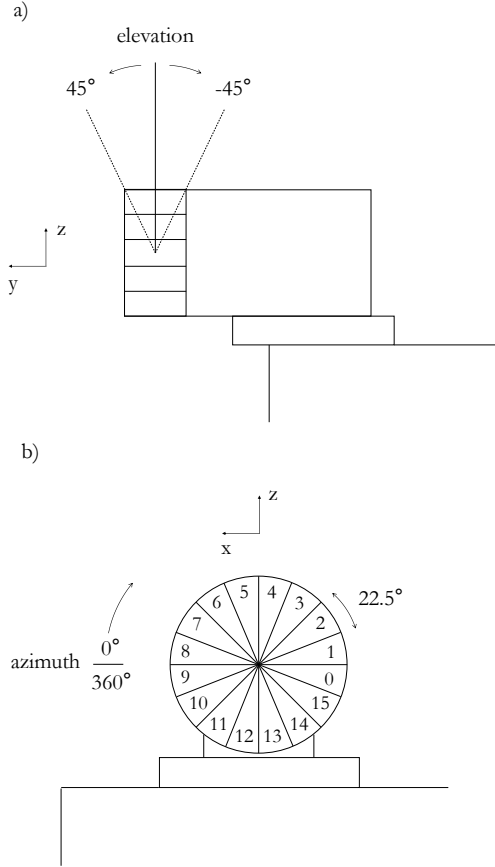
Figure 3.2: Sketch of ICA showing the definitions of a) elevation angles and
b) the 16 azimuthal sectors. Adapted from Bergman et al. (2020).

3.1.1 *Shadowing*

In Figure 3.3 the whole sky as seen from ICA is shown, with az-
imuthal angle on the x-axis and elevation angle on the y-axis. The
grid pattern illustrates the FOV of ICA, where one cell of the grid
represents one instrument pixel. The grey area shows the location of
the spacecraft. It is clear that the spacecraft and some of the other in-
struments are blocking the FOV of ICA. Sectors located on the upper
half of the instrument, i.e. sectors 1-8 (azimuth 0°-180°), are more or
less non-shadowed, while sectors located on the other side of the in-
strument (sectors 9-15 and 0, azimuth 180°-360°) are totally blocked
by the spacecraft for elevation angles below 0°. One of the solar pan-
els causes some additional shadowing for sectors 13 and 14. The solar

panels can rotate along its longest axis and shown in Figure 3.3 is one typical configuration. Other instruments on board are also partially blocking the FOV of ICA. Especially the Microwave Instrument for the Rosetta Orbiter (MIRO, Gulkis et al., 2007) and IES, but also LAP to some extent. Note that this is a simplified non-exact map of where spacecraft structures are located in the ICA FOV. It is based on a FOV map from the RO-RPC-ICA-EAICD document (Nilsson, 2019). Some manual modifications have been made to the figure to improve the accuracy, but it should still only be considered as an indication of where larger structures are located in the FOV.

Figure 3.3: The whole sky as seen from ICA, where each cell of the grid represents the FOV of one instrument pixel and the grey area shows approximately where the spacecraft is located in the FOV.

4

SPACECRAFT CHARGING

A spacecraft in space is constantly exposed to the surrounding environment. The result is a charge transfer between the spacecraft surface and the environment, charging the surface to a positive or negative potentia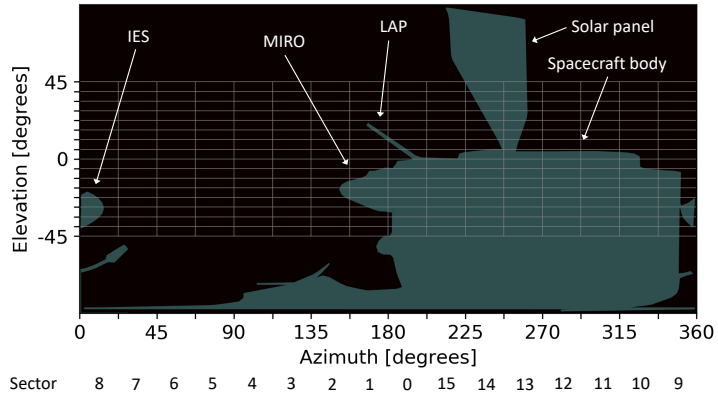l with respect to the plasma (e.g. Garrett, 1981; Whipple, 1981). The particles in the surrounding space plasma is persistently bombarding the surface. The velocity of the electrons is usually much higher than the velocity of the ions, and the electron flux to the surface will therefore exceed the ion flux, resuting in a negative charging of the surface. When the potential is low enough the electrons will start to get repelled from the surface, while the ions are being attracted. Eventually the electron and ion currents will balance and an equilibrium potential is reached. If the spacecraft is exposed to sunlight, photoemission will also contribute to the charging. Photoemission alone will result in a positive potential, due to photoelectrons leaving the surface. In such a vacuum case we will reach an equilibrium potential when the potential is high enough for the photoelectrons to be attracted back to the surface. When the spacecraft is located in a sunlit plasma, the ultimate potential is determined from a balance between the electron, ion and photoelectron current. Other currents, for example due to secondary electron emission, may also become important at times. Hence the potential of the spacecraft is determined from the current balance

$$I_e + I_i + I_{ph} + I_{other} = 0, \tag{4.1}$$

where I_e is the electron current, I_i is the ion current, I_{ph} is the photoelectron current and I_{other} is all other contributing currents. Other charging mechanisms can during certain conditions become important. One example is magnetic field induced differential potentials. When the spacecraft is moving through an ambient magnetic field a charge separation will arise due to the Lorentz force law. If the spacecraft structures are large enough this can give rise to differential charging, i.e. potential differences between different parts of the spacecraft. Another example is wake effects. A wake behind the spacecraft will fill with hot electrons, due to their high velocity. This region is hence characterized by a more negative plasma potential, an enhanced electron temperature and a decreased plasma density (e.g. Tribble, 2003). The different plasma characteristics in this region may have implications for the spacecraft charging. A third example is charging mechanisms induced by the spacecraft itself, caused by, for example, exposed high-potential surfaces and thrusters. Spacecraft charging and the related processes are hence very complicated.

4.1   THEORETICAL MODEL FOR A MAXWELLIAN PLASMA

Normally, the ion current to the spacecraft is much smaller than the electron current, and can hence be neglected. The dominating currents are then usually the electron current and the photoelectron current. For such a case, a simplified model of the resulting spacecraft potential can be derived for a Maxwellian plasma. The derivation is based on probe theory (e.g. Laframboise and Parker, 1973; Mott-Smith and Langmuir, 1926), but the same reasoning holds for a negatively charged spacecraft body. The model has been derived using *orbital-limited* theory, which means that all electrons hitting the spacecraft have to originally come from infinity (and not from i.e. another part of the spacecraft). We also assume that the velocity of the spacecraft and the bulk flow of the plasma are small compared to the thermal velocity of the electrons.

The electron current to the spacecraft surface for a negatively charged spacecraft is then given by (Odelstad et al., 2017)

$$I_e = A_{s/c} e n_e \sqrt{\frac{kT_e}{2\pi m_e}} \exp\left(\frac{eU_{s/c}}{kT_e}\right), \tag{4.2}$$

where $A_{s/c}$ is the current collecting area of the spacecraft, e is the elementary charge, n_e is the electron density, k is the Boltzmann constant, T_e is the electron temperature, m_e is the electron mass and $U_{s/c}$ is the spacecraft potential.

The factor $n_e \sqrt{\frac{kT_e}{2\pi m_e}}$ in Equation 4.2 is the random flux of electrons to the spacecraft surface, which has been obtained by integrating over the Maxwellian velocity distribution. The current to the spacecraft due to this random electron flux is found by multiplying by the total current collecting area of the spacecraft and the charge of one electron. The factor $\exp\left(\frac{eU_{s/c}}{kT_e}\right)$ is a repelling factor arising due to the negatively charged spacecraft surface.

The electron current is balanced by the photoelectron current, which usually has to be determined empirically. The balance is given by

$$I_e + I_{ph} = 0 \tag{4.3}$$

and hence

$$A_{s/c} e n_e \sqrt{\frac{kT_e}{2\pi m_e}} \exp\left(\frac{eU_{s/c}}{kT_e}\right) + I_{ph} = 0, \tag{4.4}$$

This equation can be solved for $U_{s/c}$, yielding

$$U_{s/c} = -\frac{kT_e}{e} \ln\left(\frac{A_{s/c} e n_e}{-I_{ph}} \sqrt{\frac{kT_e}{2\pi m_e}}\right). \tag{4.5}$$

Note that the currents are considered positive when flowing from the spacecraft to the plasma, and hence I_e is positive while I_{ph} is negative. Thereof the minus sign before I_{ph} in Equation 4.5.

From this equation it is clear that an enhanced electron temperature and/or electron density result in a more negative spacecraft potential. An enhanced photoelectron current does, on the contrary, result in a less negative potential. The derived relation is hence consistent with the discussion in the beginning of Chapter 4.

4.2   THE SPACECRAFT POTENTIAL OF ROSETTA

The spacecraft potential of Rosetta has been studied by Odelstad et al. (2015) and Odelstad et al. (2017), using LAP data cross-calibrated with ICA data. The LAP instrument consists of two probes mounted on booms. Details about the instrument can be found in Eriksson et al. (2007), but the basic principle of this instrument is to vary the probe potential and study the resulting collected current. From this, conclusions about parameters such as plasma density, electron temperature, drift velocity, spacecraft potential and solar EUV flux can be drawn.

To determine the spacecraft potential from LAP measurements, Odelstad et al. (2017) use two methods: *bias potential sweeps* and a *floating probe*. When doing bias potential sweeps, the potential of the probe is swept through a defined potential range, and the resulting collected current is studied. Photoelectrons are emitted from a sunlit probe, and when the probe has a negative potential with respect to the plasma, all these electrons will be repelled from the probe. When the probe potential passes the value of the plasma potential, and becomes positive, some of these photoelectons will however be attracted back to the probe. This effect is enhanced with increased probe potential, and will give rise to a characteristic current-voltage curve with a "knee" at the plasma potential. From this the spacecraft potential can be determined. When the spacecraft potential is determined from a floating probe, the probe potential is floating with the plasma. The resulting potential difference between the spacecraft and the probe is measured, and by empirically estimating the potential of the probe with respect to the plasma at the distance of the probe from the spacecraft, the value of the spacecraft potential is obtained. Due to the empirical estimate of the probe potential the uncertainty is larger when determining the spacecraft potential from a floating probe than from bias potential sweeps, but the time resolution is greatly enhanced.

The booms on which the two LAP probes are mounted are too short to place the probes entirely outside of the potential field of the spacecraft, and therefore LAP only measures a fraction of the spacecraft potential. To deal with this effect, Odelstad et al. (2017) compares the obtained values with spacecraft potential estimates made

by ICA. The lowest particle energy measured by an ion instrument placed on a negatively charged spacecraft is equal to the spacecraft potential (discussed in more detail in the next section). By studying the lower cutoff in energy in the ICA data the spacecraft potential can hence be estimated.

The conclusion from these studies is that the Rosetta spacecraft was commonly charged to a substantial negative potential of around -10 to -20 V. The negative potential is attributed to a warm electron population of 5-10 eV. The potential varies with the plasma environment throughout the mission, and strong negative potentials are typically observed close to perihelion, while a positive potential of a few volts occasionally was observed far from the comet nucleus and in regions of low cometary activity. The potential also tends to be more negative above the summer hemisphere of the comet. Generally it is also more negative above the neck region, due to a more intense outgassing in this region. An enhanced outgassing rate leads to a higher amount of neutral particles in the environment, in turn increasing the plasma density. The spacecraft potential will then be driven more negative according to Equation 4.5.

4.3 INFLUENCE ON LOW-ENERGY PLASMA MEASUREMENTS

Spacecraft charging is problematic for several reasons. Firstly, differential charging can cause discharges between different spacecraft parts, which can lead to devastating consequences for a spacecraft and the instruments on board. These effects are, however, minimized during the spacecraft design process through e.g. grounding and the usage of conducting materials. Another less investigated problem is the interference with scientific measurements. This is especially problematic for low-energy plasma measurements.

When the charged particles encounter the spacecraft, they are affected by the electric field arising around the spacecraft due to the charged surface. They are attracted to or repelled from the surface, resulting in a change in kinetic energy of the particles. The kinetic energy ΔE_k gained or lost can be easily calculated by considering the total energy conservation of kinetic energy and electric potential energy. The change in electric potential energy of a charged particle moving between two points in an electric field is defined as

$$\Delta E_U = q\Delta U, \tag{4.6}$$

where q is the charge of the particle and ΔU is the potential difference between the points. Conservation of energy implies that a change in potential energy results in a change in kinetic energy, according to

$$\Delta E_k + \Delta E_U = \text{const.} \tag{4.7}$$

In our case, the two points are the spacecraft surface and infinity. At infinity the potential is defined to be 0, and at the spacecraft surface the potential is equal to the spacecraft potential, $U_{s/c}$. The kinetic energy gained, or lost, by the particles due to the charged surface is hence given by

$$\Delta E_k = -q U_{s/c}. \tag{4.8}$$

For ion measurements the ions will hence gain (lose) an energy ΔE_k when the spacecraft potential is negative (positive). For a negative potential, this means that ions with an initial energy of 0 eV will be accelerated to an energy corresponding to the spacecraft potential, and this is hence the lowest energy measured. The advantage of this situation is that parts of the ion population that initially are below the energy range of the instrument become detectable. If the potential, on the other hand, is positive, the ions will be decelerated by the spacecraft. We then miss all ions in the population with an energy below $q U_{s/c}$, since they will not reach the instrument. These effects are only important when the energies of the measured ions are comparable to the potential of the spacecraft.

Another consequence of the attracting or repelling potential is that the low-energy particle trajectories will be affected by the field, affecting the effective FOV of the instrument (see Section 7.1 for further discussion about the distinction between nominal and effective FOV). For positive ions and a negative potential this will result in a "focusing" effect, enhancing the FOV of the instrument and, consequently, the measured flux. This will affect the geometric factor of the instrument. One example of this effect observed in ICA data is shown in Figure 4.1. In this polar plot we have the 16 sectors on the azimuthal axis, energy on the radial axis and the color scale represents detected counts. This is data obtained from one energy sweep. The time resolution in this case has been increased to 4 seconds, obtained by reducing the amount of energy steps to 32 and only using one elevation angle (close to the aperture plane). This high time resolution mode was implemented after Rosetta arrived at the comet, and the highly variable environment was realized (for more details about this mode see Stenberg Wieser et al. (2017)). In this mode we only sweep the low-energy part of the spectrum and measure energies up to ~80 eV. In Figure 6 it is clear that the angular spread of this low-energy data is very wide, ions are detected from basically all directions. This is believed to be an effect caused by the negatively charged spacecraft, attracting ions from all directions. It is clear that the FOV of the instrument is greatly enhanced in this case. Methods to theoretically correct for this effect are presented by e.g. Lavraud and Larson (2016), but generally the FOV distortion is complex and requires modelling.
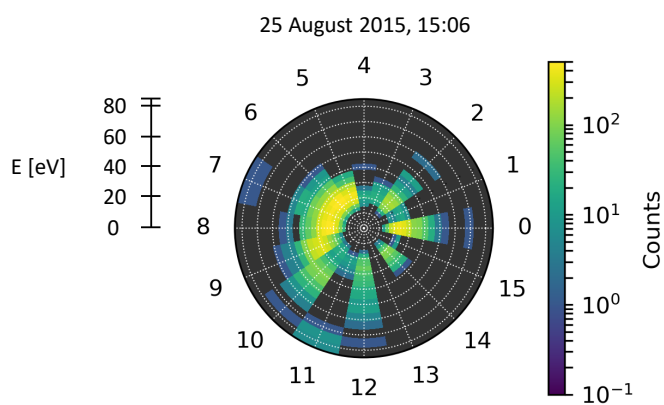
Figure 4.1: Low-energy example data from ICA obtained on 2015-08-25 15:06. The 16 sectors are on the azimuthal axis, the energy is on the radial axis and the color scale represents counts. The time resolution is 4 seconds. The wide angular spread is attributed to the negatively charged spacecraft.

LOW-ENERGY IONS AROUND 67P/CHURYUMOV-GERASIMENKO

As already mentioned, the neutral gas particles in the cometary coma get ionized and picked up by the solar wind. These processes result in several observed ion populations in the vicinity of 67P characterized by their different energies. These populations include three different cometary ion populations in addition to the solar wind populations (e.g. Berčič et al., 2018). This is illustrated in Figure 5.1 where an energy spectrogram of some typical ICA data is plotted. The solar wind ions (H^+, He^{2+} and He^+) are characterized by their high energy of more than several hundred eV. Note that He^+ is not a usual constituent of the solar wind, it is, in this case, created through charge exchange between He^{2+} and cometary particles. Only two cometary ion populations are visible in this plot, one population that has been picked up and accelerated by the solar wind and another one that has been newly produced and has yet not been accelerated. The newly born ions have initially a very low energy (a consequence of conservation of momentum), and are expanding more or less radially outward from the comet nucleus due to ambipolar fields. The expanding population is observed with energies ranging from a few eV up to 50 eV, while the accelerated population are observed up to similar energies as the solar wind. In the data we also see indications of a third cometary ion population, a local population. The local population is not visible in Figure 5.1, but consists of the ions that have just been born and hence have a very low energy. This population is characterized by a wider angular spread than the expanding population.

A large part of the ions observed in the environment around 67P have a low energy, and they hence play an important part in the cometary processes. Unfortunately, these ions have an energy in the same order of magnitude as the spacecraft potential (see Section 4.2), which makes the data difficult to interpret.
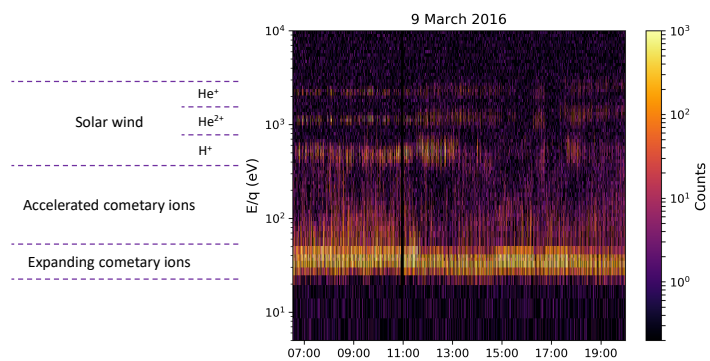
Figure 5.1: The different ion populations observed around comet 67P, shown in ICA data obtained on 2016-03-09.

SPIS SIMULATIONS

To study the influence of the spacecraft potential on the low-energy ICA data, we model the interactions between the spacecraft and the surrounding plasma. We use the Spacecraft Plasma Interaction Software (SPIS, Thiébault et al., 2013). The first version of this software was developed between the years 2002-2005, after an initiative made by the newly created Spacecraft Plasma Interaction Network in Europe (SPINE) (Roussel et al., 2008). The purpose of this network is to cooperate and share resources connected to the interactions between spacecraft and plasma. The need for a simulation tool became apparent, and a first JAVA-based prototype, PicUp3-D, was developed (Forest, Eliasson, and Hilgers, 2001). Following this first prototype, ESA made an initiative under contract with ONERA/DESP, Artenum and University Paris VII to develop the Particle-In-Cell (PIC) code which is now SPIS. Since then several new versions with improvements in terms of numerical solvers and new modules have been released, with SPIS 5.2.4 being the version used in this work.

6.1 BASIC SIMULATION PRINCIPLE

The whole simulation cycle of SPIS is illustrated in Figure 6.1. First the electromagnetic fields are computed from the charge distribution, and then particles are transported through the fields. After this the interaction with the spacecraft is modelled, including photo emission and secondary electron emission by protons and electrons. Lastly, the spacecraft potential is determined from the current balance. The cycle is then repeated by solving for the electromagnetic fields for the new charge distribution, transporting particles and solving the interactions with the surface. This is repeated until equilibrium is reached.

SPIS uses a Particle-In-Cell (PIC) method for the modelling. This model considers the movement of individual particles, and is hence capable of resolving fine structure and individual particle trajectories (as opposed to magnetohydrodynamic simulations where the plasma is treated as a fluid). The main principle of the PIC method is to compute the electromagnetic fields on the mesh in the simulation volume by solving the Maxwell equations, given by

$$\nabla \cdot \mathbf{E} = \frac{\rho_c}{\varepsilon_0}, \tag{6.1}$$

$$\nabla \times \mathbf{E} = -\frac{\partial \mathbf{B}}{\partial t}, \tag{6.2}$$

$$\nabla \cdot \mathbf{B} = 0, \tag{6.3}$$

$$\nabla \times \mathbf{B} = \mu_0 \mathbf{J} + \mu_0 \varepsilon_0 \frac{\partial \mathbf{E}}{\partial t}, \tag{6.4}$$

where $\mathbf{E}$ is the electric field, ρ_c is the current density, ε_0 is the permittivity of free space, $\mathbf{B}$ is the magnetic field, μ_0 is the permeability of free space and $\mathbf{J}$ is the current density. The magnetic field in SPIS is always constant and uniform, and hence the Poisson equation (Equation 6.1) is the only equation needed to solve for the fields in SPIS. This step corresponds to box 1 in Figure 6.1.

The particles are then moved through the resulting field by the Lorentz force (box 2 in Figure 6.1), given by

$$\mathbf{F} = q\mathbf{E} + q\mathbf{v} \times \mathbf{B}, \tag{6.5}$$

where $\mathbf{v}$ and q are the velocity and charge of the particle, respectively.

The huge amount of particles in the simulation makes it impossible to track each particle individually. Instead, so called *super particles* or *macro particles* are used. Each super particle represents several real particles with approximately the same position and velocity. The trajectory of the super particle represents the trajectory of each individual particle represented by it. In SPIS, the amount of super particles per cell (and hence the statistical properties of the simulation) can be controlled.

To reduce the complexity of the simulation and the simulation time, approximations can be made for the electrons which do not have to be modelled as PIC. Instead they are described by a Maxwell-Boltzmann thermal equilibrium distribution. This approximation is possible when the spacecraft potential is negative and no potential barriers exist.

6.2 SPACECRAFT MODEL

To accurately simulate the charging of the spacecraft and the resulting environment we need a correctly dimensioned model of the spacecraft. We also have to define the boundaries of the simulation volume, which has to be large enough for the tracked particles to not be significantly affected by the spacecraft at the external boundary (i.e. the edge of the volume). Furthermore surface material properties and the electrical configuration of the exposed spacecraft surfaces have to be defined.
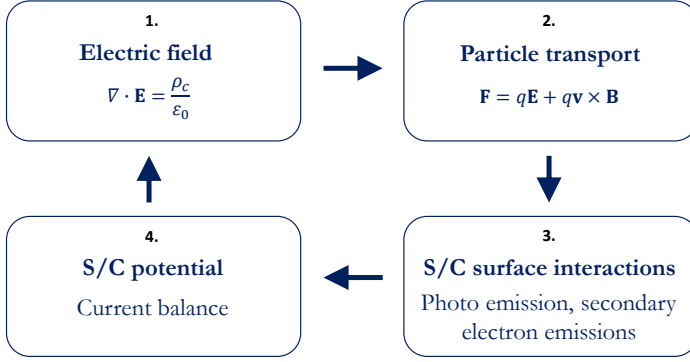
Figure 6.1: The basic simulation principle used by SPIS.

6.2.1 *Spacecraft*

The model of the spacecraft (shown to the right in Figure 6.2 and in Figure 6.3) is simplified, where the spacecraft body is a correctly dimensioned box with two solar panels. The dimensions are shown in Figure 6.3. In this model the lander, Philae, has already been released from the spacecraft. The only instruments included are ICA and LAP.

6.2.2 *Coordinate system*

SPIS uses a Cartesian coordinate system (x, y, z), which for the simulations presented in this thesis is centered at the spacecraft with the axes pointing as defined in Figure 6.2 and Figure 6.3. In this frame, Rosetta was usually positioned with the Sun in the positive x-direction and the comet in the positive z-direction. Separate local coordinate systems are defined for the scientific instruments used for the particle tracing, described in detail in Section 6.4.2.

6.2.3 *Simulation volume and meshes*

All geometric elements in SPIS are represented by simple geometries such as triangles and tetrahedra. The file format supported is the *geo Gmsh* format (Geuzaine and Remacle, 2009). This format allows for a complex modelling where the resolution of the mesh can be adapted and increased in regions were a more detailed modelling is necessary. Generally, the mesh resolution at the external boundary can be reduced considerably compared to the required resolution close to the spacecraft, without loss of accuracy in the simulation results. This reduces the computational time.

For the simulations presented in this thesis an elliptically shaped simulation volume of $70 \times 60 \times 60$ m is used. It is shown to the left

in Figure 6.2. The inner ellipse is an auxiliary surface used to control the meshing.

The cell size at the external boundary is 3 m, which is enough to resolve the potential field, while the resolution close to the spacecraft is high enough to resolve the Debye length and details in the spacecraft structure. The resolution is usually around 2 cm close to ICA and 10-25 cm for the rest of the spacecraft. It is gradually reduced from the spacecraft to the external boundary.
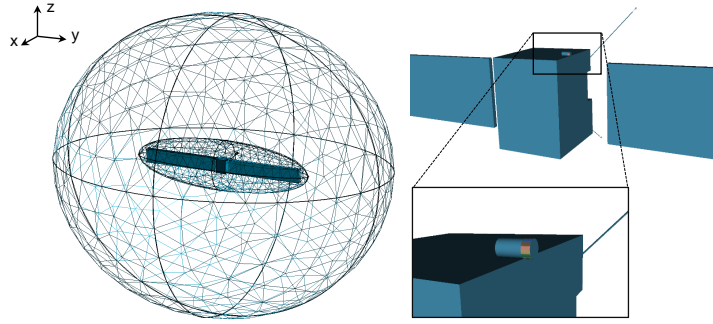
Figure 6.2: The spacecraft model used in the simulations. To the left the whole simulation volume is shown including the external boundary (with decreased mesh resolution to enhance visibility). To the right the spacecraft model and the ICA instrument is shown. Adapted from Bergman et al. (2020).
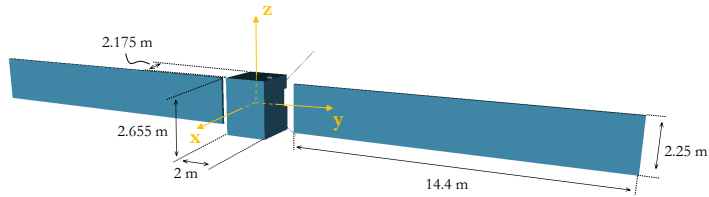
Figure 6.3: Dimensions of the spacecraft model and definition of the spacecraft coordinate system (x, y, z).

6.2.4 *Modelling of surface materials*

The characteristics of the spacecraft surfaces can be modelled using materials from the catalogues coming with the software. The characteristics of the selected material can also be edited if needed. For these simulations small variations and details in material properties

at different surfaces are assumed to give a negligible effect on the result. Large sunlit areas exhibit the dominating part of the photoemission, and these surfaces on Rosetta are covered with indium tin oxide (ITO). This material is therefore exclusively used in the model.

6.2.5 *Electrical circuit*

SPIS models differential charging by describing the spacecraft structure as an electrical circuit, where different parts of the spacecraft are defined as different electrical nodes. The connection between these nodes is controlled by placing resistors, capacitors or voltage generators between them. By default, each node floats separately with respect to the plasma. In this thesis differential charging is not considered, and all spacecraft parts are hence connected with the bias voltage between them put to zero. The whole spacecraft is consequently floating at the same potential with respect to the plasma.

6.2.6 *ICA*

The ICA instrument is modelled as a cylinder with length 23.25 cm and diameter 12 cm (see Figure 6.2). Each sector of the instrument is separately defined. This is needed for the particle tracing, described in more detail in Section 6.4.

6.2.7 *Detailed spacecraft model*

The above described spacecraft model, used for the simulations in Paper I, is simplified. As shown in Section 3.1.1 there are, however, other instruments and structures on board the spacecraft blocking the FOV of ICA. This will result in pure geometrical shadowing, which can be predicted. These structures can also affect the potential field around the spacecraft, which might lead to additional effects on the FOV of ICA. Such effects are investigated in Paper II, where we add two other instruments to the model that are known to block the FOV of ICA. These are IES and MIRO. The theoretical geometrical shadowing caused by these instruments is shown in Figure 3.3. The resulting spacecraft model, after adding these instruments, is shown in Figure 6.4. The instrument models are highly simplified, but the accuracy is enough to estimate additional FOV effects.

6.3 PLASMA MODEL AND SIMULATION ENVIRONMENT

The simulation environment is controlled through a large number of parameters. It is important to choose a valid plasma model, since the spacecraft potential is very sensitive to variations of some plasma parameters.
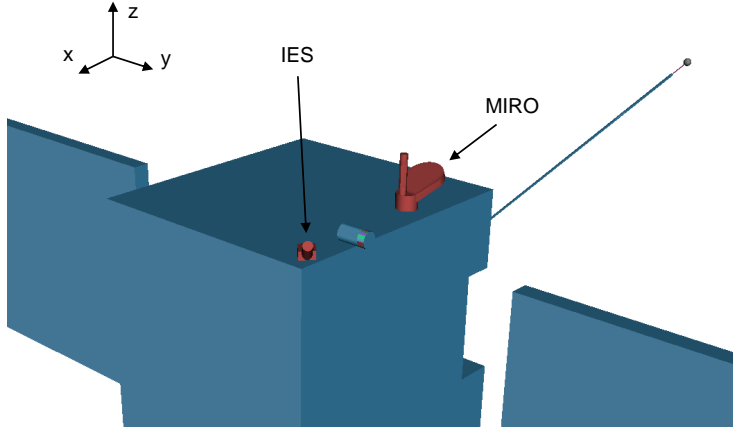
Figure 6.4: The detailed spacecraft model where IES and MIRO are added.

The plasma environment around the comet changes dramatically as the comet approaches the Sun. For the simulations in Paper I we use a plasma model representative of the environment when the comet is close to perihelion. The parameters are listed in Table 6.1, and the resulting potential field around the spacecraft is shown in Figure 6.5.

We only include cometary ions in our model, excluding the solar wind. When the comet is close to the Sun and the cometary activity is high enough, a cavity in the solar wind is created (Behar et al., 2017). This is a region where the solar wind cannot enter. When the solar wind encounters the cometary plasma, mass loading causes it to deflect due to conservation of energy and momentum (the amount gained by the cometary particles is lost by the particles in the solar wind), creating a cavity when the cometary coma is dense enough. From April 2015 until December 2015, Rosetta was inside of this cavity and the solar wind ions consequently disappeared from the ICA data. This corresponds to the studied period around perihelion. The density of the solar wind is furthermore very low ($\sim$5-10 cm^{-3}) compared to the cometary ion density (100-1500 cm^{-3}, Henri et al., 2017), and is not expected to affect the simulation results if included. Therefore, we only include cometary ions in our model.

Water group ions are dominating the environment around the comet (Fuselier et al., 2015, 2016; Nilsson et al., 2015). H_2O^+, H_3O^+, OH^+ and O^+ are all important ions, but ICA cannot distinguish between them and they are furthermore assumed to yield similar simulation results. Therefore, the simulation environment is exclusively modelled with H_2O^+. For more information about the cometary ion population used in the model, the reader is referred to Paper I.

The properties of the electron population are important for the resulting value of the spacecraft potential, and are therefore worth

Table 6.1: Plasma parameters used for the simulations presented in Paper I.

POPULATION	PARAMETER	VALUE	REFERENCE
Cometary ion population (H_2O^+)	Density [cm^{-3}]	1000	Henri et al. (2017)
	Temperature [eV]	0.5	Galand et al. (2016)
	Velocity [km/s]	4	Odelstad et al. (2018) and Vigren and Eriksson (2017)
Electron population	Density [cm^{-3}]	1000	Equal to ion density (for quasi-neutrality)
	Temperature [eV]	8	Eriksson et al. (2017)

mentioning. Two different electron populations have been reported by Eriksson et al. (2017), where one has a temperature of 5-10 eV and the other one is cold with a temperature below 0.1 eV. We only consider the warm population for our model, since the cold population is expected to give a negligible effect on the spacecraft potential. The model temperature of 8 eV is chosen considering the sensitivity of the spacecraft potential to changes in this parameter. Our model yields a potential of -21 V, which is a rather low but typical value observed close to perihelion, yielding clear particle tracing results.

No magnetic field is included in the model. As already mentioned, comet 67P does not have an intrinsic magnetic field, and the IMF is very weak and assumed to give a negligible effect on the results. The field strength is increased when the cometary activity is high, but is still usually below 40 nT (Goetz et al., 2017). The gyro radius of the ions is consequently very large, much larger than the system we are studying. We therefore assume that the studied ion trajectories would not be affected by the magnetic field.

The described plasma model is representative of the environment around the comet close to perihelion. The environment, however, varies a lot as the comet orbits the Sun. The distance of the spacecraft to the comet was furthermore varying, resulting in a changing environment around the spacecraft. Three important parameters will change as the environment changes: the potential of the spacecraft, the Debye length of the plasma and the photoemission from the spacecraft. The spacecraft potential is important for obvious reasons. The Debye length is one of the most important parameters determining the shielding properties of the spacecraft, and this parameter can therefore also be expected to affect the particle tracing results. The plasma model used in Paper I yields a Debye length of 0.66 m, but we can expect Debye lengths varying from a few tens of cm up to a few meters during the whole mission. The photoemission becomes important indirectly by altering the potential of the spacecraft and the plasma sheath close to the spacecraft. These effects are investigated in Paper II.
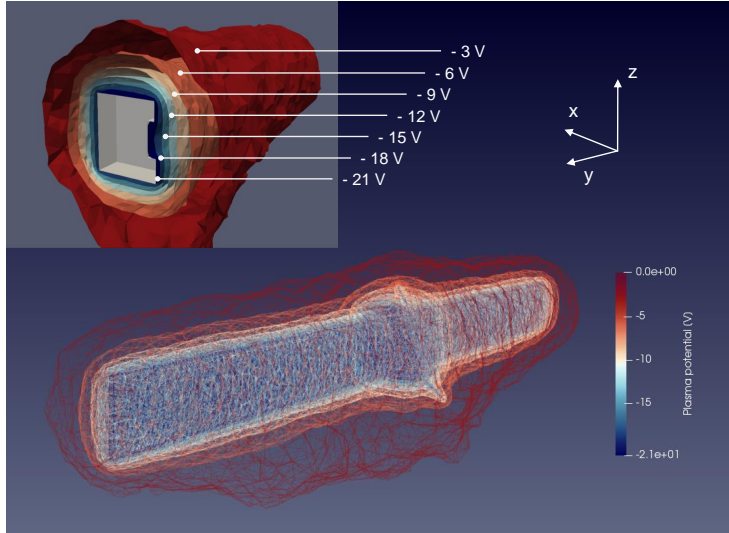
Figure 6.5: Resulting potential field around the spacecraft when the plasma model described in Table 6.1 is used. A few potential surfaces are shown. The spacecraft potential is -21 V and the Debye length is 0.66 m. Figure from Bergman et al. (2020).

6.4 PARTICLE TRACING

Scientific instruments can be added to the SPIS simulation (Matéo-Vélez, Sarrailh, and Forest, 2013). Several types of real or virtual instruments or probes are available, which all can be used for scientific analyses. One supported instrument is a particle detector. The current implementation can be used to study the distribution of particles at a defined surface area through a test particle approach. The test particle method implies that the fields are frozen before the particles are traced. In SPIS, the actual tracing is done by a series of backward and forward tracing to keep the computational load reasonable. The output is the distribution of the detected particles, both at detection location and at the external boundary where the particles originate. We use this tool to study the particles detected by ICA. Each sector of ICA is defined as a separate particle detector, where the detector is located at the aperture of the sector (see Section 6.4.3 for further discussion).

6.4.1 *Test particle populations*

By default, SPIS lacks the possibility to define the tracked particles individually. It can only be set to track one of the already existing populations in the simulation, which are defined as distributions. This is inconvenient for our application, where we want to study specific

particle energies. We solve this by defining a broad Maxwellian distribution, and afterwards processing the results to pick out the interesting energies from the distribution. To ensure energy coverage, this artificial distribution is defined with a high temperature. Since we want to study each travel direction equally, this population is also defined with zero bulk velocity.

The test particle distribution is included in the simulation environment. This is also inconvenient for our application, since the properties of this population are differing from the other ion population (described in Section 6.3). We therefore have to add one extra population to the simulation. To ensure that this population does not affect the rest of the simulation system, its density is put six orders of magnitude lower than the cometary ion population. We run test simulations in SPIS where we do and do not include this test population, and the results show that this population does not noticeably affect the resulting plasma potential, and is assumed to give a negligible effect on the system.

6.4.2 *Coordinate system and acceptance angles*

The particle tracing tool in SPIS uses a reference frame different from the spacecraft coordinate system (x, y, z). Two different frames are used for the instrument: one to present the simulation results and one to define the orientation of detector surfaces and acceptance angles. Matéo-Vélez, Sarrailh, and Forest (2013) use the notation (x_0, y_0, z_0) and (x_d, y_d, z_d) for these frames, and for convenience we will use the same notation here. The (x_0, y_0, z_0) frame is defined by defining an origin using (x, y, z) coordinates, and then rotating the system when necessary. The (x_d, y_d, z_d) frame is defined by rotation of the (x_0, y_0, z_0) frame. More specifically, the basis is first rotated around z_0 with an angle θ_d to obtain a transitional basis $(x', y', z' = z_0)$, and the final (x_d, y_d, z_d) basis is obtained by rotation around the transitional axis y' with an angle φ_d. z_d has to point towards the backside of the detector surface, and acceptance angles (defining the nominal FOV) are defined symmetrically around z_d as two angles $\pm\alpha$ and $\pm\beta$, in the plane (x_d, z_d) and (y_d, z_d) respectively. In our case, the (x_0, y_0, z_0) frame is defined in the same way as (x, y, z), but with the origin at the center of the aperture plane of the instrument. In Paper I we distinguish between whole sector simulations and individual pixel simulations, where whole sector simulations study the whole sectors without dividing into the different elevation bins, and individual pixel simulations study one elevation bin of one sector. For individual pixel simulations the (x_0, y_0, z_0) system has to be rotated to simplify the definition of (x_d, y_d, z_d). Both cases are illustrated in Figure 6.6. Note that the two different (x_0, y_0, z_0) frames are chosen out of convenience, and differs from the prevalent system for ICA. The (x_d, y_d, z_d) frame is different for each sector or pixel, but

the principle is illustrated in Figure 6.7 for both whole sector and individual pixel simulations. The resulting systems for one randomly chosen sector and pixel are shown. Note that only half of the total FOV is shown ($2\alpha \times 2\beta$ in total, symmetrically around z_d). Note also that α is used to define azimuthal angle for the whole sector case, and β defines elevation angle. For the individual pixel case the situation is reversed, α defines elevation angle and β defines azimuthal angle. This is due to the complex rotation of the reference frame necessary for the individual pixel simulations, where also the elevation angle has to be considered.

6.4.3 *Detector area*

A simplified instrument model is used for the simulations, where the aperture area of each sector is defined as a detector. The actual design of the instrument results in different effective entrance areas for each elevation bin. This is not taken into account. All particles hitting the defined detector area within the acceptance angles are considered detected, which results in a larger effective entrance area than for the real instrument. This is, however, assumed to give a negligible effect on the results considering the small detector areas compared to the size of other spacecraft structures and the normalization of the resulting flux.

6.4.4 *Elevation bins*

As already mentioned, the elevation range of ICA is divided into 16 elevation bins with a resolution of 5.625°. The elevation angle of the center of each elevation bin is energy dependent and varies with energy step and the software version used in the instrument. To reduce the amount of simulation cases we choose one setup where one elevation bin is centered at the aperture plane, and the rest is equally distributed on each side, spaced by 5.625°. For this setup, the use of 16 elevation steps is inconvenient since it yields an uneven distribution for elevations above and below 0°. We therefore add one extra elevation bin. The outermost elevation bins are then centered at +45° and -45°, as illustrated in Figure 3.2a. When using the simulation results to correct actual data, the results have to be interpolated to fit the studied case.
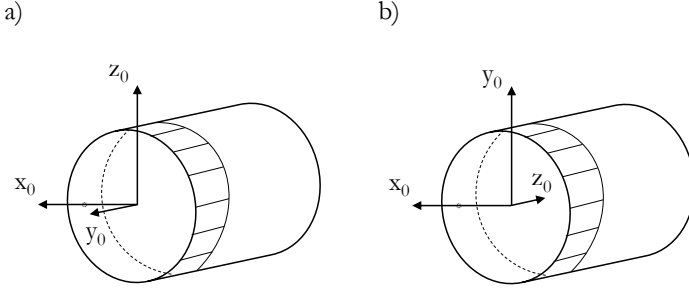
Figure 6.6: Definition of the (x_0, y_0, z_0) frame used for a) whole sector simulations and b) individual pixel simulations.
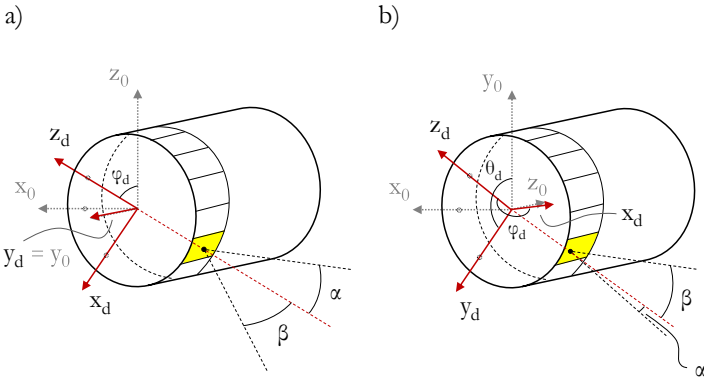

Figure 6.7: Definition of the (x_d, y_d, z_d) frame used for a) whole sector simulations and b) individual pixel simulations. The frame is differently defined for each sector/pixel, shown is the frame for one random sector/pixel. Also shown is how the acceptance angles α and β are defined in these frames.

6.4.5 *OcTree algorithm*

SPIS uses an OcTree algorithm to optimize the internal representation of the velocity distribution during the particle tracing process. An OcTree algorithm uses a tree data structure to divide 3D space. Space is subdivided into octants, and each octant can in turn be divided into eight new octants. The principle is illustrated in Figure 6.8. Each region can be further divided as much as necessary. By doing this, SPIS can enhance the resolution in regions where a finer structure is necessary, and through this refine the distribution.

The maximum number of OcTree created and the maximum number of particles backtracked can be controlled. By default, they are set to 10000 and 100000 respectively, but are for the simulations presented in this thesis increased to 100000 and 1000000. This gives a reasonable compromise between resolution and simulation time.
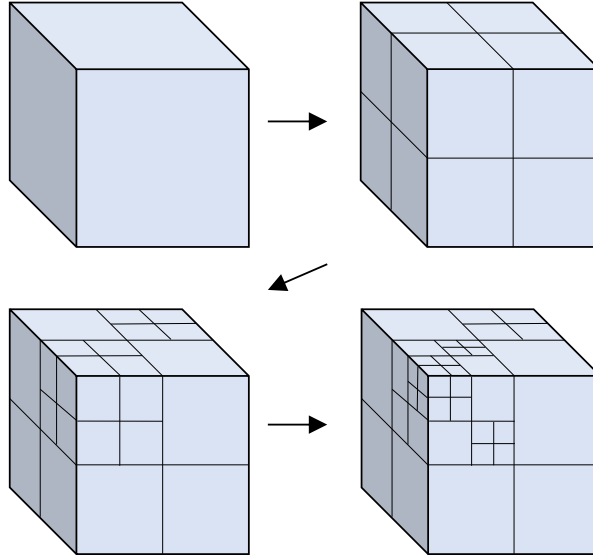

Figure 6.8: General principle of how an OcTree algorithm divides space into octants. In volumes divided into smaller boxes finer structures can be resolved.

6.5   PROCESSING OF SPIS OUTPUT

SPIS presents the particle tracing results as a discrete velocity distribution, both at the external boundary and at detection location. The velocity limits of the distribution are determined from the energy limits for the instrument set in SPIS, and the resolution in velocity for each axis is determined from the number of energy steps. We convert these velocity distributions to flux and travel direction. The velocity distribution is expressed in the (x_0, y_0, z_0) frame (i.e. Cartesian coordinates), and we need a conversion to the system used by ICA. This is illustrated in Figure 6.9. We only show the conversion for the (x_0, y_0, z_0) frame used for whole sector simulations (see Figure 6.6), but the results yielded by individual pixel simulations can easily be trans-

lated into this frame through rotation. The travel direction expressed in azimuth and elevation angles is calculated according to

$$\theta = \cos^{-1}\left(\frac{v_x}{\sqrt{v_x^2 + v_z^2}}\right), \tag{6.6}$$

$$\varphi = \sin^{-1}\left(\frac{v_y}{\sqrt{v_x^2 + v_y^2 + v_z^2}}\right). \tag{6.7}$$
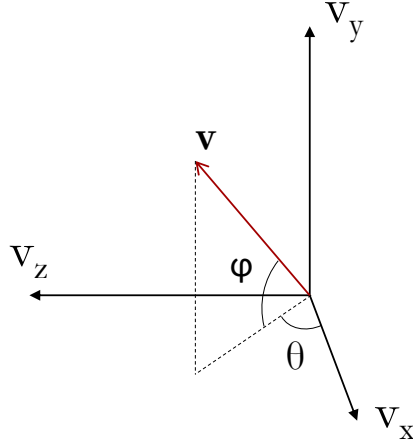

Figure 6.9: Conversion from Cartesian coordinates to travel direction in the system used by ICA.

The flux is given by the second moment of the velocity distribution function:

$$F = \int v f(v) d^3 v, \tag{6.8}$$

where $f(v)$ is the velocity distribution provided by SPIS (in units of $s^3 m^{-6}$) and v is the velocity. We want to study the flux for one given energy interval and direction, and express the flux per solid angle. When this is considered, together with the fact that our distribution is discrete, the integral becomes the sum

$$F_{\theta,\varphi} = \sum_n \frac{v_r f(n, \varphi, \theta) \Delta v_r \Delta v_\varphi \Delta v_\theta}{\Delta \Omega}, \qquad n = v_1, v_1 + \Delta v_r ... v_2 \tag{6.9}$$

where $F_{\theta,\varphi}$ is the flux in the direction (θ, φ) within an energy interval defined by the velocity limits v_1 and v_2 and $\Delta\Omega$ is the solid angle subtended by the pixel. This is illustrated in Figure 6.10, and we deduce (assuming that Δv_r, Δv_φ and Δv_θ are sufficiently small) that

$$\Delta v_r = \Delta v, \tag{6.10}$$

$$\Delta v_\varphi = v_r \Delta\varphi, \tag{6.11}$$

$$\Delta v_\theta = v_r \cos(\varphi)\Delta\theta, \tag{6.12}$$

and the solid angle is given by

$$\Delta\Omega = \cos(\varphi)\Delta\varphi\Delta\theta. \tag{6.13}$$

This yields flux in units of $\mathrm{m^{-2}s^{-1}sr^{-1}}$.

Due to the discrete velocity distribution, values are only available for certain directions with gaps in between. To smooth out the distribution and the resulting flux map, linear interpolation is used between the points in the distribution.
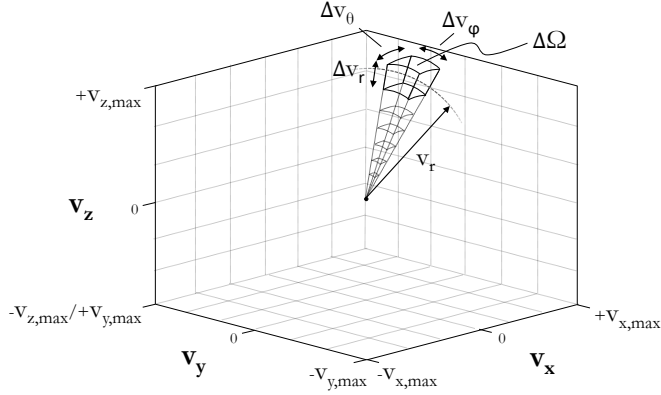

Figure 6.10: The principle of calculating the flux from a certain direction from the velocity distribution.

7

7.1 NOMINAL AND EFFECTIVE FIELD OF VIEW

An important definition used in the appended papers is the separation between *nominal* and *effective* (or *actual*) FOV. The *nominal* FOV is defined by the instrument hardware. It is the FOV determined during instrument ground calibration. This FOV is independent of the environment the instrument is later placed in. The *effective* FOV is the resulting FOV when environmental effects are also taken into consideration, in our case the potential field caused by the charged spacecraft. We then consider the environment around the spacecraft as an extension of our instrument, and the effective FOV corresponds to the FOV of this whole extended system. At high energies the effective FOV coincides with the nominal FOV, due to the limited influence of the potential field on these ions, but at low energies the effective FOV may differ substantially from the nominal.

7.2 DESCRIPTION OF FIELD OF VIEW PLOTS

All SPIS results presented in the appended papers are presented as flux maps, similar to the example shown in Figure 7.1. All discussions in this thesis are based on these plots, and therefore a thorough description of them is appropriate. These plots represent the whole sky, as seen from ICA. Azimuthal angle is on the x-axis and elevation angle is on the y-axis. The dashed square represents the nominal FOV of the studied part of the instrument (elevation bin 9 of sector 2 in Figure 7.1). All particles will have a travel direction within this square at detection. The colored area, on the other hand, represents the effective FOV of this part of the instrument for the corresponding energy interval. The color scale shows the flux of particles at the external boundary that is reaching the studied part of the instrument from different directions. This has been calculated from the SPIS output as described in Section 6.5. The colored area of the plot hence shows where the particles are actually coming from, and a brighter area in the plot means that more particles are coming from this direction. Nominally, the colored area would coincide perfectly with the dashed square, meaning that the particles have the same travel direction at the external boundary as at the detection location. From Figure 7.1, however, it is clear that this is not the case for low energies. When the energy is higher the effective FOV approaches the nominal FOV, while it at lower energies spreads out and changes position. The color scale has been normalized with respect to the maximum

flux for each individual case. The reader should be aware that, in terms of flux, the plots are not comparable due to this individual normalization. The reader should also be aware of the equirectangular projection, which, together with the unit of $m^{-2}s^{-1}sr^{-1}$, enlarges the poles of the plot. This effect is similar to the one enlarging the landmasses close to the poles on a world map.

In a similar way, we can produce plots showing the travel direction of the particles at the detection location. This can be used to study shadowing effects. One example is shown in Figure 7.2. Here the result for all elevation angles of sector 14 are shown in the same plot. The dashed square represents the nominal FOV of this whole sector. The color scale still corresponds to flux, but is now representing the flux of particles at detection. For a non-shadowed sector, the colored area fills the whole dashed square. In Figure 7.2, it is clear that this is not the case for sector 14. The reason is that the spacecraft body and the solar panel are shadowing this sector (c.f. Figure 3.3). These type of plots are therefore used to study different shadowing effects.
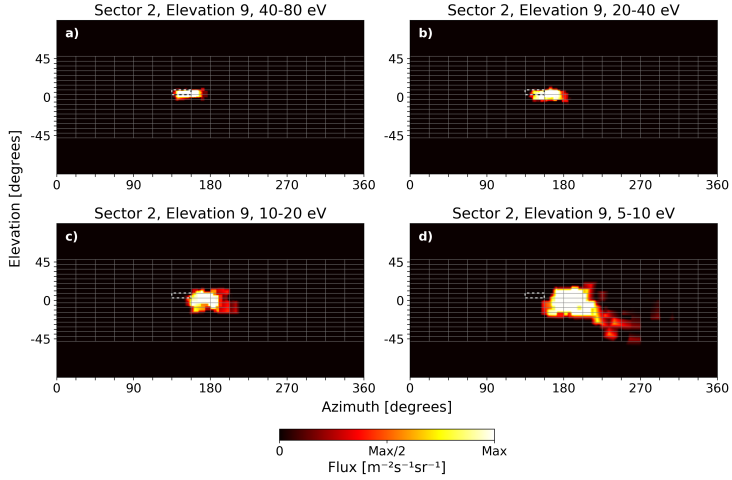

Figure 7.1: Example of flux maps showing the particle tracing results. Azimuthal angle is on the x-axis and elevation angle is on the y-axis. The dashed square represents the nominal FOV of the studied pixel, while the colored area shows where the detected particles are originally coming from. The color scale represents flux of particles at the external boundary reaching the detector. Four different energy intervals are shown (corresponding to energy at the external boundary): a) 40-80 eV, b) 20-40 eV, c) 10-20 eV and d) 5-10 eV. The spacecraft potential is -21 V.
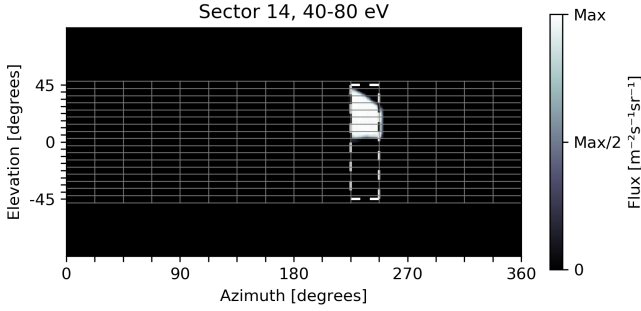
Figure 7.2: Example of a flux map showing the travel direction of the ions at detection for one complete sector. The dashed square represents the nominal FOV of the sector. The energy interval is the energy of the ions at the external boundary.

7.3 LIMITATIONS AND NUMERICAL ARTEFACTS

The numerical solver of SPIS poses limitations on the accuracy of the simulation results. For example, to reach reasonable simulation times, parameters such as amount of test particles, grid resolution, OcTree division and amount of energy steps have to be limited. These parameters are also limited by the amount of available memory.

The SPIS potential solver also has accuracy limitations, causing "noise" in the potential field. One example is shown in Figure 7.3, where potential surfaces around the spacecraft from one simulation are plotted. The potential surfaces around the spacecraft exhibit wiggles (especially the outermost surface in Figure 7.3), which are caused by the uncertainty of the solver. This noise in turn affects the particle tracing results for low energies, causing a wider spread. To avoid this effect we do not study ion energies below 5 eV, which we judge to be below the accuracy limit.

As described in Section 6.5, the particle tracing results are presented as discrete velocity distributions. The resolution (i.e. the amount of bins for each axis) is determined from the energy resolution of the instrument. In our case, the instrument is set to detect particles from 0 to 200 eV with a step size of 0.5 eV. This results in a velocity distribution matrix of $400 \times 400 \times 400$ elements. Each axis is then evenly binned in velocity (not energy), causing equally sized bins in velocity space. When converting this to angular coordinates, the resulting effect is that bins located close to the center of the distribution cover a larger angle than bins located further away. This is illustrated with a two dimensional example in Figure 7.4. Two pixels with absolute velocities v_1 and v_2 where $v_1 < v_2$ are plotted together with their angular coverages ω_1 and ω_2. It is clear that pixel 1 covers a much larger angle when transforming to angular coordinates, which is due to the even binning in velocity. In the flux maps showing the simu-

lation results this causes numerical artefacts for low energies. A few examples are shown in Figure 7.5. Areas with circular, quadrangular or triangular shapes are caused by this effect. This in combination with the noise effect previously described can cause these shapes to appear at random positions in the plots. Luckily they are easy to distinguish due to their characteristic shapes, and can be filtered away.
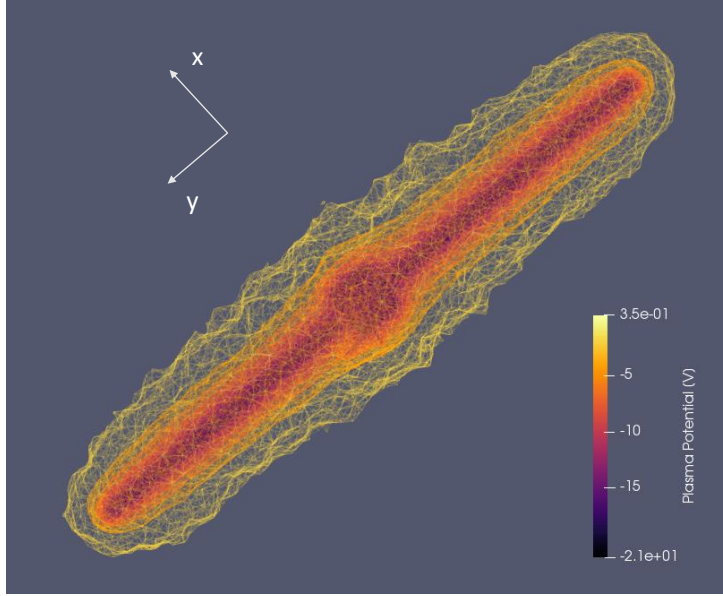

Figure 7.3: Example output from SPIS, showing the potential field around the spacecraft. "Noise" in the potential field is clearly visible for the outermost potential surface.
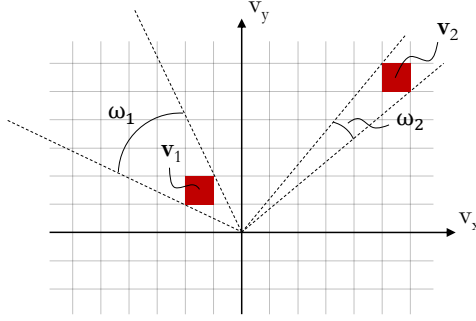
Figure 7.4: Illustration of one of the effects causing numerical artefacts at low energies.
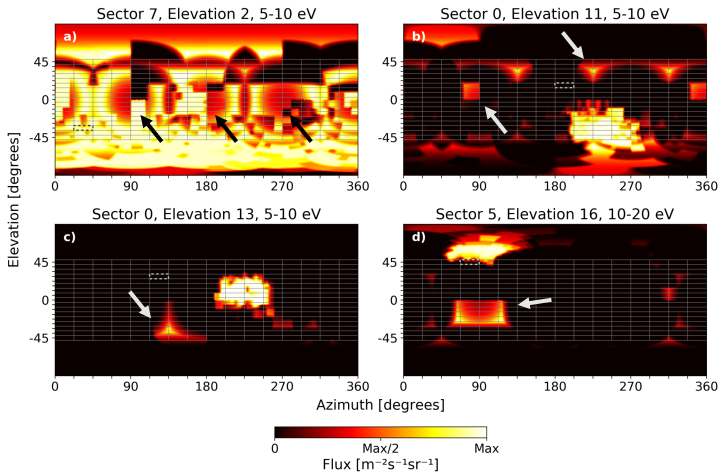
Figure 7.5: Example of a few numerical artefacts appearing in the simulation results.

7.4   UNCERTAINTY ESTIMATION

The SPIS solver uses Monte Carlo elements, involving a random sampling of initial values of particle positions and velocities from the user defined distributions. Consequently, the simulation results will exhibit statistical variations (i.e. two simulations with identical setups will not yield identical results). Unfortunately, the resulting uncertainty level is unknown for SPIS. To estimate this level, we run 18 simulations with the same plasma conditions and geometry, but varying randomly selected particles, for a few instrument pixels. The different results are then used to estimate the uncertainty.

In Figure 7.6 an example for one of the instrument pixels is shown when the plasma model from Paper I is used. First, we take the results from the 18 simulations and create FOV plots as previously described. We then take all 18 plots and calculate the mean value of the flux for each pixel in the plot. The result for sector 3, elevation 8, is shown in panel a-d for four different energy intervals. By calculating the mean flux for each direction and creating a new average plot of the FOV, we reduce uncertainties and get a smooth FOV plot without artefacts caused by statistical variations. For detailed calculations where precise information about the FOV is needed, this approach should be used to reduce the uncertainty. To study the uncertainty level, we also calculate the standard deviation of each pixel in the plot. The result is plotted in panel e-h. Brighter areas in the plot means a larger variation within the 18 simulations. For all energy intervals the standard deviation is low at the center of the FOV, while the uncertainty is larger at the edges. This is as expected. It is also clear that the uncertainty in FOV position is reduced when we increase the energy of the ions. This is also as expected since high-energy ions are not affected by the potential field (and hence uncertainties in the potential field) to the same extent as low-energy ions.

The simulation results presented in this thesis yield important information about how the FOV grows in size at lower ion energies. This information is, for example, important when determining the geometric factor at low energies. However, the SPIS uncertainty level results in an uncertainty in the estimation of the size of the FOV. The 18 simulations can be used to estimate also this uncertainty. In Figure 7.7 the result for sector 3, elevation 8, is once again shown. The dashed vertical lines correspond to the mean value of all 18 simulations for each energy interval, and the arrows show the variation. The ends of the arrows correspond to the minimum and maximum value, and the thicker part of the arrow corresponds to the region covered by the standard deviation. As already concluded, it is clear that the uncertainty increases with lower energies.
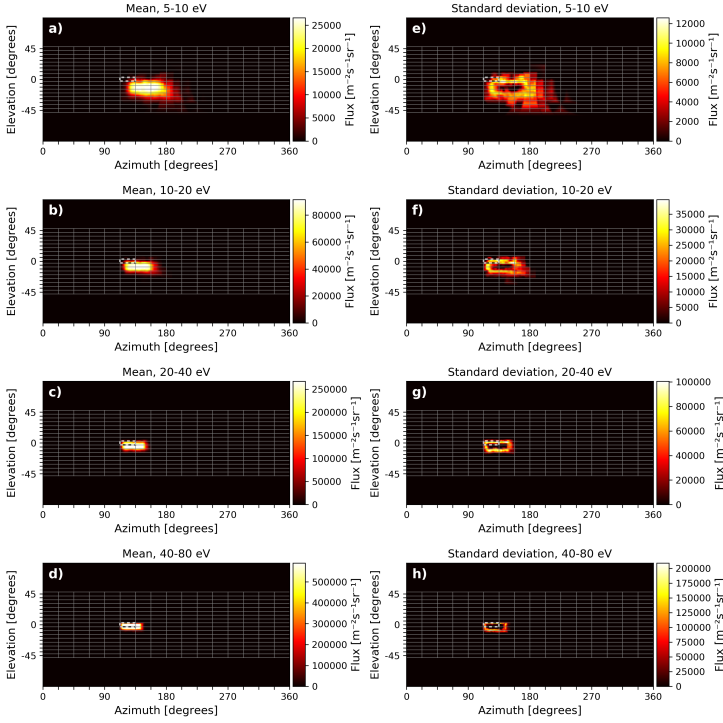
Figure 7.6: Plots produced by combining 18 simulations to improve the statistics. In a)-d) the mean flux for each direction is plotted, and in e)-h) the corresponding standard deviation.
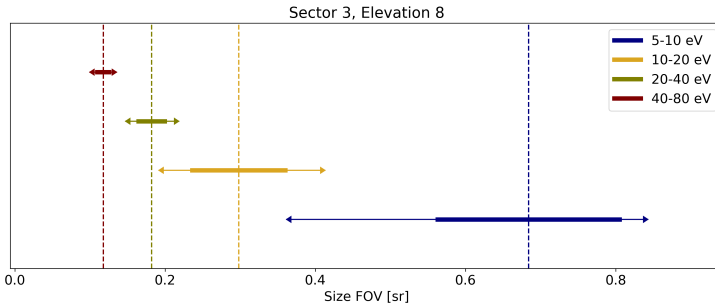
Figure 7.7: Example of an uncertainty estimate of the FOV size made for one instrument pixel. 18 simulations are used for the estimation. The different colors represent different energy intervals. The thicker part of the arrows corresponds to the region located within the standard deviation, and the ends of the arrows show the obtained minimum and maximum value. The FOV size has been calculated by summing up all plot pixels with a flux more than 10% of the pixel with the maximum flux.

8

CONCLUSIONS AND FUTURE WORK

The results presented in this thesis make up an important first step towards to goal of reconstructing the low-energy data obtained with ICA. The next step will be to recalculate the geometric factor for low-energies, taking into consideration the different FOVs for different instrument pixels. Then the method will be applied to actual data, which will make it possible to study the directional part of the low-energy ICA data for the first time.

SPIS has some limitations for our application, but the software has nonetheless turned out to be a very helpful tool yielding satisfactory results. The greatest limitation is the noise level, which limits the accuracy at low particle energies and also puts constraints on the energies that can be studied.

Even though the work is focused on ICA, the method can be adapted to other instruments on other spacecraft. One important factor is the spacecraft geometry and the position of the instrument with respect to the spacecraft body. If this differs significantly from Rosetta, new simulations with a new spacecraft model should be run. Otherwise the results presented here can be used to make rough estimates of what the situation might be for other spacecraft with different spacecraft potentials and plasmas.

Low-energy ions have been shown important for the understanding of many environments; the importance for cometary science presented in this thesis is far from exclusive. This work can hopefully pave the way for future studies that can further enhance the understanding of the spacecraft potential induced distortions of low-energy ion (and electron) data. This will be an important next step towards properly understanding processes involving low-energy particles.

9

PAPER I

Bergman, S., Stenberg Wieser, G., Wieser, M., Johansson, F. L., & Eriksson, A. (2020). The influence of spacecraft charging on low-energy ion measurements made by RPC-ICA on Rosetta. *Journal of Geophysical Research: Space Physics*, 125(1). doi:10.1029/2019JA027478

In the first paper we use SPIS to analyze the FOV distortion of ICA at ion energies down to 5 eV. We use one specific plasma model, valid when the comet is close to perihelion and yielding a spacecraft potential of -21 V. Results for all instrument pixels are provided. The results show that the FOV is severely distorted at the lowest energies, but the distortion varies between different viewing directions. Generally, pixels with extreme elevation angles are more severely distorted than those close to the aperture plane. However, sectors located on one half of the instrument generally behave differently than those located on the other half, due to the shadowing of the spacecraft. For sectors 9-12 pixels with high elevation angles are, for example, less distorted. The situation is hence strongly geometry dependent. All pixels grow to at least 50°×25° at low energies (5-10 eV), which is a considerable increase compared to the nominal FOV of 22.5°×5.625°. For some sectors we observe some additional shadowing effects at low energies due to the distorted FOV, mainly appearing at low elevations for sectors located on top of the instrument. Generally, the FOV is not significantly distorted when the ion energy corresponds to at least twice the spacecraft potential.

PAPER II

Bergman, S., Stenberg Wieser, G., Wieser, M., Johansson, F. L., & Eriksson, A. (2020). The influence of varying spacecraft potentials and Debye lengths on in situ low-energy ion measurements. Submitted to *Journal of Geophysical Research: Space Physics*

The second paper investigates the sensitivity of the results from Paper I to varying spacecraft potentials and Debye lengths. Generally, the FOV distortion will change when the spacecraft potential changes. In this paper we investigate whether this change is linear or not, i.e. if the same ratio between ion energy and spacecraft potential yields the same FOV distortion, independent of the value of the spacecraft potential. We fix the potential at -40 and -10 V, and compare the results to the results from Paper I. The results indicate that

a small non-linearity exists, mainly caused by the photoemission and the bulk flow of the cometary ions. However, it mainly affects the lowest energies and the size (not position) of the FOV, and can for many applications be neglected. We also investigate the sensitivity of the FOV distortion to varying Debye lengths of the surrounding plasma, which is done by keeping the potential at -21 V while varying the plasma environment to yield Debye lengths varying from 0.34 to 3.4 m. The results indicate that the FOV distortion is strongly dependent on the Debye length, where a short Debye length generally results in a more severe FOV distortion. The sensitivity varies between different viewing directions. A few pixels are not significantly affected by a changing Debye length, while the FOV of others can grow with as much as 1000% if the Debye length is decreased from 0.66 to 0.34 m.

BIBLIOGRAPHY

Auster, Hans-Ulrich et al. (2015). "The nonmagnetic nucleus of comet 67P/Churyumov-Gerasimenko." In: *Science* 349.6247. DOI: 10.1126/science.aaa5102.

Behar, E., H. Nilsson, M. Alho, C. Goetz, and B. Tsurutani (2017). "The birth and growth of a solar wind cavity around a comet – Rosetta observations." In: *Monthly Notices of the Royal Astronomical Society* 469, S396–S403. DOI: 10.1093/mnras/stx1871.

Berčič, L., E. Behar, H. Nilsson, G. Nicolaou, G. Stenberg Wieser, M. Wieser, and C. Goetz (2018). "Cometary ion dynamics observed in the close vicinity of comet 67P/Churyumov-Gerasimenko during the intermediate activity period." In: *A&A* 613, A57. DOI: 10.1051/0004-6361/201732082.

Bergman, Sofia, Gabriella Stenberg Wieser, Martin Wieser, Fredrik Leffe Johansson, and Anders Eriksson (2020). "The Influence of Spacecraft Charging on Low-Energy Ion Measurements Made by RPC-ICA on Rosetta." In: *Journal of Geophysical Research: Space Physics* 125.1, e2019JA027478. DOI: 10.1029/2019JA027478.

Burch, J. L., R. Goldstein, T. E. Cravens, W. C. Gibson, R. N. Lundin, C. J. Pollock, J. D. Winningham, and D. T. Young (2007). "RPC-IES: The Ion and Electron Sensor of the Rosetta Plasma Consortium." In: *Space Science Reviews* 128, pp. 697–712. DOI: 10.1007/s11214-006-9002-4.

Capaccioni, F. et al. (2015). "The organic-rich surface of comet 67P/Churyumov-Gerasimenko as seen by VIRTIS/Rosetta." In: *Science* 347.6220. DOI: 10.1126/science.aaa0628.

Carr, C. et al. (2007). "RPC: The Rosetta Plasma Consortium." In: *Space Science Reviews* 128.1, pp. 629–647. DOI: 10.1007/s11214-006-9136-4.

Cravens, T. and T. Gombosi (2004). "Cometary magnetospheres: a tutorial." In: *Advances in Space Research* 33.11, pp. 1968–1976. DOI: 10.1016/j.asr.2003.07.053.

Eriksson, A. I. et al. (2007). "RPC-LAP: The Rosetta Langmuir Probe Instrument." In: *Space Science Reviews* 128, pp. 729–744. DOI: 10.1007/s11214-006-9002-4.

Eriksson, A. I. et al. (2017). "Cold and warm electrons at comet 67P/Churyumov-Gerasimenko." In: *A&A* 605, A15. DOI: 10.1051/0004-6361/201630159.

Festou, M. C., H. Rickman, and R. M. West (1993). "Comets." In: *The Astronomy and Astrophysics Review* 4.4, pp. 363–447. DOI: 10.1007/BF00872944.

Forest, J., L. Eliasson, and A. Hilgers (2001). "A New Spacecraft Plasma Simulation Software, PicUp3D/SPIS." In: *Spacecraft Charg-*

ing Technology. Ed. by R. A. Harris. Vol. 476. ESA Special Publication, p. 515.

Fuselier, S. A. et al. (2015). "ROSINA/DFMS and IES observations of 67P: Ion-neutral chemistry in the coma of a weakly outgassing comet." In: *A&A* 583, A2. DOI: 10.1051/0004-6361/201526210.

Fuselier, S. A. et al. (2016). "Ion chemistry in the coma of comet 67P near perihelion." In: *Monthly Notices of the Royal Astronomical Society* 462, S67–S77. DOI: 10.1093/mnras/stw2149.

Galand, M. et al. (2016). "Ionospheric plasma of comet 67P probed by Rosetta at 3 au from the Sun." In: *Monthly Notices of the Royal Astronomical Society* 462, S331–S351. DOI: 10.1093/mnras/stw2891.

Garrett, Henry Berry (1981). "The charging of spacecraft surfaces." In: *Reviews of Geophysics* 19.4, pp. 577–616. DOI: 10.1029/RG019i004p00577.

Geuzaine, Christophe and Jean-François Remacle (2009). "Gmsh: A 3-D finite element mesh generator with built-in pre- and post-processing facilities." In: *International Journal for Numerical Methods in Engineering* 79.11, pp. 1309–1331. DOI: 10.1002/nme.2579.

Glassmeier, Karl-Heinz, Hermann Boehnhardt, Detlef Koschny, Ekkehard Kührt, and Ingo Richter (2007a). "The Rosetta Mimssion: Flying towards the origin of the Solar System." In: *Space Science Reviews* 128, pp. 1–21. DOI: 10.1007/s11214-006-9140-8.

Glassmeier, Karl-Heinz et al. (2007b). "RPC-MAG The Fluxgate Magnetometer in the ROSETTA Plasma Consortium." In: *Space Science Reviews* 128, pp. 649–670. DOI: 10.1007/s11214-006-9114-x.

Goetz, C. et al. (2016a). "First detection of a diamagnetic cavity at comet 67P/Churyumov-Gerasimenko." In: *A&A* 588, A24. DOI: 10.1051/0004-6361/201527728.

Goetz, C. et al. (2016b). "Structure and evolution of the diamagnetic cavity at comet 67P/Churyumov–Gerasimenko." In: *Monthly Notices of the Royal Astronomical Society* 462, S459–S467. DOI: 10.1093/mnras/stw3148.

Goetz, Charlotte, Martin Volwerk, Ingo Richter, and Karl-Heinz Glassmeier (June 2017). "Evolution of the magnetic field at comet 67P/Churyumov–Gerasimenko." In: *Monthly Notices of the Royal Astronomical Society* 469, S268–S275. DOI: 10.1093/mnras/stx1570.

Gulkis, S. et al. (2007). "MIRO: Microwave Instrument for Rosetta Orbiter." In: *Space Science Reviews* 128.1, pp. 561–597. DOI: 10.1007/s11214-006-9032-y.

Henri, P. et al. (2017). "Diamagnetic region(s): structure of the unmagnetized plasma around Comet 67P/CG." In: *Monthly Notices of the Royal Astronomical Society* 469, S372–S379. DOI: 10.1093/mnras/stx1540.

Johnson, Charles Y. and Edith B. Meadows (1955). "First investigation of ambient positive-ion composition to 219 km by rocket-borne spectrometer." In: *Journal of Geophysical Research (1896-1977)* 60.2, pp. 193–203. DOI: 10.1029/JZ060i002p00193.

Laframboise, J. G. and L. W. Parker (1973). "Probe design for orbit-limited current collection." In: *The Physics of Fluids* 16.5, pp. 629–636. DOI: 10.1063/1.1694398.

Lavraud, Benoit and Davin E. Larson (2016). "Correcting moments of in situ particle distribution functions for spacecraft electrostatic charging." In: *Journal of Geophysical Research: Space Physics* 121.9, pp. 8462–8474. DOI: 10.1002/2016JA022591.

Matéo-Vélez, J.-C., P. Sarrailh, and J. Forest (2013). *User Manual-Annex 2-Advanced use for scientific applications.*

Meierhenrich, U. (2015). *Comets and their Origin: The Tool to Decipher a Comet.* Weinheim, Germany: Wiley-VCH. ISBN: 978-3-527-41281-5.

Mott-Smith, H. M. and Irving Langmuir (1926). "The Theory of Collectors in Gaseous Discharges." In: *Phys. Rev.* 28 (4), pp. 727–763. DOI: 10.1103/PhysRev.28.727.

Nilsson, H. et al. (2007). "RPC-ICA: The Ion Composition Analyzer of the Rosetta Plasma Consortium." In: *Space Science Reviews* 128, pp. 671–695. DOI: 10.1007/s11214-006-9031-z.

Nilsson, Hans (2019). *Experimenter to (Science) Archive Interface Control Document, RO-RPC-ICA-EAICD.* Tech. rep.

Nilsson, Hans et al. (2015). "Birth of a comet magnetosphere: A spring of water ions." In: *Science* 347.6220. DOI: 10.1126/science.aaa0571.

Odelstad, E., A. I. Eriksson, N. J. T. Edberg, F. Johansson, E. Vigren, M. André, C.-Y. Tzou, C. Carr, and E. Cupido (2015). "Evolution of the plasma environment of comet 67P from spacecraft potential measurements by the Rosetta Langmuir probe instrument." In: *Geophysical Research Letters* 42.23, pp. 10,126–10,134. DOI: 10.1002/2015GL066599.

Odelstad, E., A. I. Eriksson, F. L. Johansson, E. Vigren, P. Henri, N. Gilet, K. L. Heritier, X. Vallières, M. Rubin, and M. André (2018). "Ion Velocity and Electron Temperature Inside and Around the Diamagnetic Cavity of Comet 67P." In: *Journal of Geophysical Research: Space Physics* 123.7, pp. 5870–5893. DOI: 10.1029/2018JA025542.

Odelstad, Elias, G. Stenberg-Wieser, M. Wieser, A. I. Eriksson, H. Nilsson, and F. L. Johansson (2017). "Measurements of the electrostatic potential of Rosetta at comet 67P." In: *Monthly Notices of the Royal Astronomical Society* 469, S568–S581. DOI: 10.1093/mnras/stx2232.

Roussel, J., F. Rogier, G. Dufour, J. Mateo-Velez, J. Forest, A. Hilgers, D. Rodgers, L. Girard, and D. Payan (2008). "SPIS Open-Source Code: Methods, Capabilities, Achievements, and Prospects." In: *IEEE Transactions on Plasma Science* 36.5, pp. 2360–2368. DOI: 10.1109/TPS.2008.2002327.

Stenberg Wieser, Gabriella et al. (2017). "Investigating short-time-scale variations in cometary ions around comet 67P." In: *Monthly Notices of the Royal Astronomical Society* 469, S522–S534. DOI: 10.1093/mnras/stx2133.

Szegö, Károly et al. (2000). "Physics of Mass Loaded Plasmas." In: *Space Science Reviews* 94.3, pp. 429–671. DOI: 10.1023/A:1026568530975.

Thiébault, B., J.-C. Mateo-Velez, J. Forest, and P. Sarrailh (2013). *SPIS 5.1 User Manual*.

Tribble, Alan C. (2003). *The space environment: Implications for spacecraft design*. Revised and expanded ed. Princeton, New Jersey: Princeton University Press.

Trotignon, J. G. et al. (2007). "RPC-MIP: the Mutual Impedance Probe of the Rosetta Plasma Consortium." In: *Space Science Reviews* 128, pp. 713–728. DOI: 10.1007/s11214-006-9005-1.

Vigren, E. and A. I. Eriksson (2017). "A 1D Model of Radial Ion Motion Interrupted by Ion-Neutral Interactions in a Cometary Coma." In: *The Astronomical Journal* 153.4, p. 150. DOI: 10.3847/1538-3881/aa6006.

Whipple, E C (1981). "Potentials of surfaces in space." In: *Reports on Progress in Physics* 44.11, pp. 1197–1250. DOI: 10.1088/0034-4885/44/11/002.